Automatic intracranial space segmentation for Computed Tomography brain images

C. Adamson[1], A. Da Costa[2,3], R. Beare[1,4], A. G. Wood[3,4,5,*]

[*] Corresponding author: (a.g.wood@bham.ac.uk)
School of Psychology
University of Birmingham
Edgbaston B15 2TT
United Kingdom
+44 121 414 3338

[1]*Developmental Imaging, Murdoch Childrens Research Institute, Parkville, Australia*
[2]*Department of Plastic and Maxillofacial Surgery, The Royal Children's Hospital, Melbourne, Australia.*
[3]*Australian Centre for Child Neuropsychology Studies, Murdoch Childrens Research Institute, Melbourne, Australia.*
[4]*Department of Medicine, Southern Clinical School, Monash University, Melbourne, Australia.*
[5]*School of Psychology, University of Birmingham.*

Abstract

Craniofacial disorders are routinely diagnosed using Computed Tomography (CT) imaging. Corrective surgery is often performed early in life to restore the skull to a more normal shape. In order to quantitatively assess the shape change due to surgery, we present an automated method for intracranial space segmentation. The method utilises a two-stage approach which firstly initialises the segmentation with a cascade of mathematical morphology operations. This segmentation is then refined with a level-set based approach that ensures that low-contrast boundaries, where bone is absent, are completed smoothly. We demonstrate this method on a dataset of 43 images and show that the method produces consistent and accurate results.

Keywords: Intracranial space segmentation, Computed Tomography, Level set methods, Mathematical morphology.

Automatic intracranial space segmentation for Computed Tomography brain images

Abstract

Craniofacial disorders are routinely diagnosed using Computed Tomography (CT) imaging. Corrective surgery is often performed early in life to restore the skull to a more normal shape. In order to quantitatively assess the shape and volume change of the ICS due to surgery, we present an automated method for intracranial space segmentation. The method utilizes a two-stage approach that initializes the segmentation with a cascade of mathematical morphology operations. This segmentation is then refined with a level-set based approach that ensures that low-contrast boundaries, where bone is absent, are completed smoothly. We demonstrate this method on a dataset of 43 images and show that the method produces consistent and accurate results when compared to the reliability of twice repeated manual "ground truth" segmentations.

Keywords: Intracranial space segmentation, Computed Tomography, Level set methods, Mathematical morphology.

Introduction

Given its high contrast-to-noise ratio for bone and soft tissue, Computed Tomography (CT) imaging is routinely used as a diagnostic tool for craniofacial disorders. Craniofacial disorders, the most common being craniosynostosis, are a group of deformities in the growth patterns of the skull and facial bones, which are reflected in the abnormal geometry of the intracranial space (ICS). A pre-operative scan is commonly acquired for diagnostic purposes. A post-operative imaging may be performed in order to assess the efficacy of the surgical technique in restoring a more normal ICS shape. In order to quantitatively evaluate changes in shape, a segmentation method for CT images is required. An accurate ICS segmentation is also useful for measuring intracranial volume.

The ICS is defined as the volume enclosed by the frontal, occipital, sphenoid and ethmoid bones, and two each of the parietal and temporal bones of the skull [1]. Figure 1(i) shows an example brain CT image with the ICS boundary shown in orthogonal planes. The challenging part of ICS segmentation is that the ICS is not enclosed by a continuous, high-contrast border due to

features such as the fontanelles and the foramen magnum (see Figure 1(ii)). Ideally, an ICS segmentation method would smoothly interpolate over boundary segments with no or little contrast.

Intracranial image segmentation techniques for CT images include semi-automated region growing [2], intensity thresholding [3, 4] and automated level set methods [5, 6]. Region growing methods initialize segmentation within the brain and expand segmentation boundary until high contrast edges, the skull, are reached. In regions without contrast region growing methods are prone to "leaking", where the segmentation boundary penetrates into background voxels or into the brainstem or both. In cases where segmentation leakage has occurred, manual editing was performed to correct errors. Manual editing is not reproducible, tedious and time consuming for large datasets and thus an automated method is desirable. The level set methods proposed by [5, 6] were region growing approaches that contained facilities to limit the curvature of the segmentation boundary and limit segmentation leakage. Both [5] and [6] were concerned only with fontanelle completion, which is only a portion of an ICS segmentation method. The former utilized a template-based approach where the novel image was registered to a completely closed skull whose inner boundaries were used to limit the expansion of the segmentation estimate within the fontanelles of the novel image. This method has limitations in that it requires accurate alignment of the novel image to the template, which may not occur due to the frequently unusual shape of the disordered skull. The approach of [6] is data driven and uses a curvature limiting approach to complete the fontanelles with surfaces with minimal curvature. Although the fontanelles were completed satisfactorily, which was the goal of the method, neither of the inferior boundaries of the intracranial space or the basion/opisthion axis were identified correctly.

In this paper, we propose a processing pipeline that draws on the existing techniques of mathematical morphology and level set methods and constitutes a fully automated method for intracranial space segmentation in CT images. This algorithm operates in two sequentially executed phases, which are: (i) a conservative ICS segmentation estimate and a bone tissue segmentation using a novel cascade of grayscale intensity thresholding, binary mathematical morphology and connected component operations, and (ii) refinement of the initial segmentation by smoothing the segmentation along low-contrast segments of the image, where bone is absent, in order to approximate the assumed smooth geometry of the ICS boundary. For the second phase we utilized a modified version of the illusory surfaces method of [7], which employed a level set technique that drove the segmentation boundary towards the inner boundaries of segmented objects while completing missing borders smoothly. This method utilizes a similar

curvature limiting mechanism to [6], however we modify the method to include a provision to prevent the segmentation boundary from leaking in to the brainstem. The main contribution of the method is a fully automatic, complete intracranial space segmentation procedure for CT images that uses level set method that prevents leakage of the segmentation boundary into the brainstem and completes fontanelle regions in a biologically plausible manner.

Materials and method

In this section we present our multi-step algorithm for segmenting the intracranial space from a brain CT image. The method employs 2 sequentially executed phases:

(i) Construct an initial conservative segmentation, bone and brainstem segmentations with intensity-based thresholds and mathematical morphology operations, and

(ii) Refine the segmentation boundary so that missing edges in the bone segmentation image are completed smoothly with the illusory surfaces method.

We now describe our method for constructing s_{init}, s_{bone} and $s_{\mathrm{brainstem}}$, which denote the initial ICS segmentation, the bone segmentation and the brainstem segmentation, respectively. A block diagram of this procedure is shown in Figure 2.

We generated an initial segmentation of the CT brain image, using histogram analysis, into four classes, which were: air (background), s_{air}, a low intensity tissue class that is predominantly composed of voxels within connective tissue beneath the skin and orbital fat, $s_{\mathrm{tissue,low}}$, a high intensity tissue class whose voxels represent the brain, the eyes, the skin and extra ocular muscle tissue, $s_{\mathrm{tissue,high}}$, and bone, s_{bone}. Figure 3(i) shows a histogram of a typical image from our dataset. This histogram is largely bi-modal with the lower intensity peak representing air or background voxels and the higher intensity peak representing high intensity tissue voxels. Dominant peak detection was performed by finding zero-valued residuals after subtracting the dilated histogram from the original. Non-dominant peaks, those with histogram values of less than 1%, were discarded. We employed the heuristic of defining the $s_{\mathrm{tissue,low}}/s_{\mathrm{tissue,high}}$ and the $s_{\mathrm{tissue,high}}/s_{\mathrm{bone}}$ thresholds by the start points of the valleys surrounding the $s_{\mathrm{tissue,high}}$ peak. The start points of the valleys were estimated purely from the second derivative of the histogram (see

Figure 3(ii)), according to the first sub-threshold values of the second derivative after the first second derivative peaks. Finally, the $s_{\text{air}}/s_{\text{tissue,low}}$ threshold was heuristically chosen to be halfway between the s_{air} and $s_{\text{tissue,high}}$ peaks. Figure 4(ii) shows the output of this procedure applied to Figure 1(i), from our dataset.

We process the segmentation of the high intensity tissue voxels, $s_{\text{tissue,high}}$, with a sequence of binary mathematical morphology operations to produce $s_{\text{brainstem}}$ and s_{init}. Mathematical morphology provides the two basic operators of dilation and erosion, which take a structuring element (SE) and grow or shrink a binary segmentation, respectively. We utilize a spherical structuring element of a heuristically determined parameterized radius, α, to apply a modified binary opening operation to separate the ICS region from the skin, the eyes and extra ocular muscle tissue. Ideally, α would be the smallest value required to remove non-brain portions of the segmentation.

A standard opening is erosion followed by dilation. This modified opening retains only the largest connected component, denoted $\text{MaxForeground}(\cdot)$, after the erosion. Thus, we produce the intermediate segmentation, s_{opened}, which is defined as follows:

$$s_{\text{opened}} = \text{MaxForeground}(s_{\text{tissue,high}} \bigcirc R_\alpha) \oplus R_\alpha, \qquad (1)$$

An example s_{opened} is shown in Figure 4(iii).

The parameter α is chosen heuristically. Equation (1) was evaluated with α taking sequentially increasing integer starting from 4mm. We evaluate (1) for α_1 and $\alpha_2 = \alpha_1 + 1$ and calculate the volume of s_{opened} for these two values. The difference in volumes s_{opened} for α_1 and α_2 will be smallest when non-brain tissue has already been removed. Thus, we choose the lowest value of α_1 where the volume reduction of s_{opened} does not exceed a predefined threshold.

The segmentation s_{opened} is processed to form $s_{\text{brainstem}}$ followed by s_{init}. Given an axial slice orientation the brainstem portion of s_{opened} will manifest as a thin column in the inferior most slices of the image. In order to partition s_{opened} into a brainstem component $s_{\text{brainstem}}$ and s_{init}, we identify $s_{\text{brainstem}}$ by we perform slice-by-slice opening with a 2D disk shaped SE of radius 2mm, which was empirically chosen. This process is required to terminate at the first brain containing slice of the segmentation is reached. Given that the brain portion of the segmentation begins to occupy a much greater area of the axial plane at the superior extremity of the brainstem, the on process will fail to delete many voxels in this slice. Thus, the erosion process

terminates when the number of voxels not deleted by the erosion exceeds a predefined threshold. The voxels that were deleted during this process are labeled as belonging to $s_{\text{brainstem}}$, whilst voxels not deleted, including those in unprocessed slices, are labeled as s_{init}. The complete set of output segmentation images: $s_{\text{brainstem}}$, s_{init} and s_{bone} are shown in Figure 4(iv).

We now describe the refinement step that drives the boundary of the initial segmentation s_{init} towards the inner cavity of the bone segmentation s_{bone} and smoothly completes the missing segments. Prior to introducing the method, we introduce some notation. Let s_{ics} denote the current ICS segmentation estimate and let ϕ and d denote *signed distance functions* with respect to the boundaries of s_{ics} and s_{bone}, respectively. Then, we applied the variational technique proposed by [7], which was based on minimizing the following two-term energy functional:

$$E(\phi) = E_1(\phi) + E_2(\phi). \tag{2}$$

The first term, E_1, represents the discrepancy between the segmentation boundary and the inner surface of the bone segmentation and is defined as follows:

$$E_1(\phi) = \int_{\Omega} \left[|d| \delta(\phi) |\nabla \phi| + \lambda H(\phi) H(d) \right], \tag{3}$$

where λ is a positive, user-specified, scalar parameter, $H(\cdot)$ is the Heaviside function, $\delta(\cdot)$ is the Dirac delta function. The first term in (3) represents the cumulative distance between the segmentation boundary and object boundaries, whilst the second term penalizes intersections between the segmentation boundary and the image objects. By minimizing (3), the segmentation boundary is driven towards the inner surface of the bone segmentation.

The second term of (2) represents the weighted surface area of the segmentation:

$$E_2(\phi) = \beta \int_{\Omega} \delta(\phi) |\nabla \phi|, \tag{4}$$

with β being a positive weighting parameter. Minimizing (4) will produce a segmentation surface that completes the missing segments between segmented bone regions using surfaces with minimal area.

Thus, combining (3), and (4) into (2) we arrive at the following energy functional:

$$E(\phi) = \int_{\Omega} \left[|d|\delta(\phi)|\nabla\phi| + \lambda H(\phi)H(d) + \beta\delta(\phi)|\nabla\phi| \right]. \tag{5}$$

In order to minimize (5), the zero level set of ϕ evolves according to its *Euler-Lagrange* equation, which is defined as:

$$\phi_t = \delta(\phi)\left[\nabla|d| \cdot \frac{\nabla\phi}{|\nabla\phi|} + (|d| + \beta)\nabla \cdot \frac{\nabla\phi}{|\nabla\phi|} - \lambda H(d) \right] \tag{6}$$

where ϕ_t denotes the derivative of ϕ with respect to an artificial "time" variable t.

Due to the presence of $\delta(\phi)$, equation (6) only describes the movement of the zero level set of ϕ. In order to describe the evolution of all the level sets of ϕ, we replace $\delta(\phi)$ with $|\nabla\phi|$, as per [8]:

$$\phi_t = |\nabla\phi|\left[\nabla|d| \cdot \frac{\nabla\phi}{|\nabla\phi|} + (|d| + \beta)\nabla \cdot \frac{\nabla\phi}{|\nabla\phi|} - \lambda H(d) \right], \tag{7}$$

$$= \nabla|d| \cdot \nabla\phi + (|d| + \beta)\nabla \cdot \frac{\nabla\phi}{|\nabla\phi|}|\nabla\phi| - \lambda H(d)|\nabla\phi|, \tag{8}$$

The convection term, $\nabla|d| \cdot \nabla\phi$, is the main force that drives the segmentation boundary towards the bone boundaries. However, this term alone fails to direct the segmentation boundary into highly concave regions of the inner bone surfaces [9]. To rectify this, we follow [7] and introduce the acceleration factor

$$A(d) = 1 + \mu\kappa_G^+(d), \tag{9}$$

where μ is a positive parameter and $\kappa_G^+(d)$ denotes the positive component of the Gaussian curvature of d. We introduce a modulating factor, $B_{\text{brainstem}}$,

$$B_{\text{brainstem}} = 1 - 1_{s_{\text{brainstem}}} \tag{10}$$

where $1_{s_{\text{brainstem}}}$ denotes an indicator function on $s_{\text{brainstem}}$, and apply this to $A(d)$ so that the segmentation boundary is unable to penetrate inferiorly into the brainstem. Thus, the original evolution equation (8) becomes

$$\phi_t = B_{\text{brainstem}} A(d) \nabla |d| \cdot \nabla \phi + (|d| + \beta) \nabla \cdot \frac{\nabla \phi}{|\nabla \phi|} |\nabla \phi| - \lambda H(d) |\nabla \phi|. \quad (11)$$

This partial differential equation describes the motion of the segmentation boundary where the convection term (the first term) drives the segmentation boundary towards the segmented bone boundaries, the advection term (the second term) smoothes the segmentation boundary and the diffusion term (the third term) forces the segmentation boundary to the inner surface of the segmented bone region boundaries.

Dataset description

A total of 25 subjects (19 males), diagnosed with isolated sagittal synostosis, were imaged on a Siemens Sensation 16 CT scanner both prior to (mean age at first scan $\pm$ std in days; 288.9 $\pm$ 316.8) and after (mean age at second scan $\pm$ std in days; 605 $\pm$ 363.5) corrective surgery. Seven images had to be discarded since they had insufficient coverage of the brain, skull and brainstem, yielding a dataset of 43 CT images. The scans were separated by surgery and were, on average, separated by 1 year. Thus, the shape of the brain and skull evolved due to surgery and normal development for that period of life. The two images were therefore sufficiently different so that they could be interpreted as independent for validation purposes. The images had an in-plane resolution of $0.3\text{mm} \times 0.3\text{mm}$ and a slice thickness of 0.7mm. The reconstruction algorithm was chosen to optimize contrast between bone and other tissue.

Validation

Manual ICS segmentations were generated by two operators (CA and SB), together producing 2 repeated segmentations per image, using the computer assisted 3D drawing program ITK-SNAP [10]. Accuracy of automated segmentation was estimated by computing the Hausdorff distance, which is the maximal Euclidean distance between vertices on tessellated surface versions of the manual "ground truth" and the automated segmentation.

Results

We applied the processing stream of mathematical morphology, illusory surfaces and surface-based segmentation smoothing to generate estimated intracranial space segmentations for the dataset previously described.

Figure 5 shows the results of applying the illusory surfaces algorithm to a representative selection of images. It is evident that the initial segmentation boundaries are at their correct positions where bone is present, and these boundaries have been largely unchanged. The annotations highlight regions where the segmentation boundary has been changed by the illusory surfaces method. The segmentation boundary that is annotated by the curved lines (the frontal fontanelles) in Figures 6(i) and (ii) has been slightly contracted and smoothed in order to achieve a more desirable less curved completion. The asterisk in Figure 6(ii) highlights a region where the segmentation boundary has re-penetrated into a highly curved region after being initially truncated by the morphological operators. Finally, the arrows in Figures 6(i), (ii), and (iii) highlight regions of the segmentation boundary near the brainstems that have been smoothed. Additionally, the brainstem barrier functions prevented the segmentation boundaries expanding inferiorly into the brainstem.

In order to quantitatively assess the accuracy of the algorithm, we conducted a parameter sweep with respect to the illusory surface method parameters: μ and β (see Table 1). Other parameters were kept fixed: $\lambda = 5$. Algorithm accuracy was quantified by computing the Hausdorff distance (HD). Table 2 shows the mean, minimum and maximum HD for each parameter combination across all images in the dataset. Note that the HD values between the ground truth segmentations and the preprocessed segmentations, i.e. before illusory contours, were [mean (min, max): 9.35mm (4.24mm, 25.09mm)] for the first set of manual segmentations and [mean (min, max): 9.32 (3.60, 25.23)]. Thus, the computational load of the illusory contours method is justified given that it improves the accuracy of the segmentation over the preprocessing method.

The smoothing parameter β exerted the most influence on mean segmentation error. The algorithm is robust to parameter choices with any combination of $\beta < 5$ and $\mu < 40$ yielding, on average, a HD of approximately 6-8mm. The poorest average segmentation results occurred when the μ *to* β ratio was lowest. Figure 6 shows the qualitative effects of choosing extreme values of the parameters μ and β on the midsagittal slices of images that highlighted the expected effects. Choosing a large value of β caused high error values by over-smoothing and globally contracting the segmentation boundary away from the bone boundaries,

as illustrated in Figure 6(i). This effect is particularly severe in highly curved skull regions, such as the orbits (see Figure 6(i)), where excessive smoothing creates a more prominent effect. Normally μ is chosen to be much larger than β, however, the value of μ was purposefully chosen to be small for this figure to ensure the effect of an over inflated smoothing term was evident. The majority of HD values originated from segmentation errors near the foramen magnum (see Figure 6(ii) for an example).

In order to determine the variance of the segmentation boundaries compared to manual operators we computed the HD values between the two manual segmentations for each image. The HD values between the manual segmentations was [mean (min, max): 4.07 (2.02, 7.55)]. The mean errors of the automated segmentation results, see Table 2, are on the upper extreme of the range of variation between the manual segmentations. However, the accuracy of the automated segmentations is comparable to the variation seen across manual segmentations, demonstrating that the automated method is comparable in accuracy to manual operators.

Figure 7(i) shows the segmentation result for the image that yielded the highest error values across most parameter choices. Here, the pitch angle of the head was sufficient to make the brainstem detection method prematurely terminate. Therefore, the estimated location of the ICS in the brainstem is well below the desired location of the foramen magnum. After rotation of the basion/opisthion axis to the axial plane the brainstem detection component of the algorithm gave an accurate result and the error was corrected, see Figure 7(ii).

Discussion

We have presented an ICS segmentation approach for CT images, which was demonstrated and validated using a dataset consisting of 43 image volumes. The algorithm consisted of two phases: (i) generation of an initial ICS segmentation, a bone and a brainstem segmentation with a cascade of morphological operations and (ii) refinement of the ICS segmentation with the illusory surfaces method. We developed a modified version of the illusory surfaces method proposed by [7], that used a brainstem segmentation, obtained in the first stage of the algorithm, to construct a barrier term that deactivated the convection term. The purpose of this term was to prevent the segmentation boundary penetrating past the desired location of the foramen magnum.

Although the differences between the initial segmentation and the illusory surfaces output were often minor, the illusory surfaces algorithm ensured the smoothness of the segmentation boundary where bone was absent, restored the segmentation in highly curved regions of the skull and maintained the correct positions of regions of the segmentation boundary that were already at their desired locations. The smooth completion of the segmentation boundary in the absence of bone led to a biologically plausible and intuitive ICS segmentation result. The illusory surfaces method refines the initial segmentation estimate so that the geometry of the segmentation boundary in missing areas of bone were consistent regardless of bone geometry.

We remark that the shape of the sections between bone boundaries were curved rather than flat patches as dictated by the energy functional. This was, in fact, the more desirable outcome since flat patches would form a linear segment between the fontanelle boundaries and the segmentation result would have been truncated rather than following the natural curvature of the skull. This may be explained because the acceleration term is highest in highly curved bone regions, which is not the case in the fontanelles. Therefore, the evolution of the segmentation boundaries is driven more so by the advection term, which performs smoothing.

We quantitatively validated the accuracy of the algorithm by computing the Hausdorff distance, which is the maximal Euclidean distance between the estimated and ground truth segmentation surfaces. The algorithm was accurate across most parameter choices, with an average HD of approximately 6mm. The worst case segmentation errors occurred most consistently in close proximity to the foramen magnum. The severity of the error depended on the orientation of the skull with the worst-case error produced by a single image that featured a skull that was significantly pitched (see Figure 7(i)). This error was caused by a premature termination of the brainstem detection technique due to severe pitch in the head orientation. By reorienting the skull so that the basion/opisthion axis was oriented approximately in the axial plane, this error was corrected (see Figure 7(ii)). The negative effects of undesirable head orientation may be minimized manually by rotation of the head prior as a preprocessing step to ensure that the basion and opisthion are level. Automatic realignment of the input CT brain image to an appropriately oriented template may also be possible.

Conclusion

The proposed ICS segmentation method is able to construct ICS boundary representations that are comparable in accuracy to human operators. The automated nature of the algorithm significantly reduces the time needed to process large datasets. This has enormous potential for clinical research trials in which quantitative approaches are desired. For example, surgery for sagittal synostosis focuses on correcting the anterior-posterior elongation of the skull to restore a more rounded shape. However, occipital protuberances often remain after surgery. This method could quantify the "severity" of the occipital protuberance between different surgical procedures used for calvarial vault remodeling. More generally, our method can be used in prospective studies that assess the efficacy and outcomes of surgical techniques that perform corrective surgery.

There is scope for further work on this method. The obliqueness of the basion/opisthion axis compared to the axial plane affected the accuracy of the brainstem detection procedure. Further work will involve automatic alignment of the basion/opisthion axis to the axial plane prior to preprocessing.

References

1. Martini R, Ober W, Garrison C, Welch K, Hutchings RT: Fundamentals of Anatomy and Physiology:195, 2001
2. Kamdar MR, Gomez RA, Ascherman JA: Intracranial Volumes in a Large Series of Healthy Children. Plastic and Reconstructive Surgery 124:2072-2075, 2009
3. Mardini S, See LC, Lo LJ, Salgado CJ, Chen YR: Intracranial space, brain, and cerebrospinal fluid volume measurements obtained with the aid of three-dimensional computerized tomography in patients with and without Crouzon syndrome. Journal of Neurosurgery 103:238-246, 2005
4. Strik HM, et al.: Three-dimensional reconstruction and volumetry of intracranial haemorrhage and its mass effect. Neuroradiology 47:417 - 424, 2005
5. Jafarian N, et al.: Automatic fontanel extraction from newborns' CT-images using a model based level set method. Proc. 17th Iranian Conference of Biomedical Engineering (ICBME): Isfahan

6. Kazemi K, et al.: Automatic Fontanel Extraction from Newborns' CT Images Using Variational Level Set. Proc. Proceedings of the 13th International Conference on Computer Analysis of Images and Patterns Berlin, Heidelberg
7. Dong B, Chien A, Mao Y, Ye J, Osher S: Level Set Based Surface Capturing in 3D Medical Images, 2008
8. Osher S, Fedkiw R: Level Set Methods and Dynamic Implicit Surfaces, 2003
9. Zhu W, Chan W: A Variational Model for Capturing Illusory Contours Using Curvature. Journal of Mathematical Imaging and Vision 27:27-40, 2007
10. Yushkevich PA, et al.: User-guided 3D active contour segmentation of anatomical structures: Significantly improved efficiency and reliability. NeuroImage 31:1116-1128, 2006

Figure legends

Figure 1: Orthogonal views of an example CT image (i) with the intracranial space boundary marked with white contours. (ii) Midsagittal slice taken from the same CT image with the frontal fontanelle and the basion and opisthion, which are used to demarcate the foramen magnum, annotated.

Figure 2: Flowchart of mathematical morphology preprocessing steps in order to transform the input CT image into the three output segmentation images:s_{bone}, s_{init}, and $s_{\mathrm{brainstem}}$.

Figure 3: Illustration of threshold selection technique on a histogram of typical image in our dataset (i). The air/background and high intensity tissue peaks are annotated with asterisks, along with the $s_{\mathrm{air}}/s_{\mathrm{tissue,low}}$ threshold. (ii) A subset of the original histogram and its second derivative. The first sub-threshold second derivative value, after the first peak in second derivative, on the negative and positive side are used to choose the $s_{\mathrm{tissue,low}}/s_{\mathrm{tissue,high}}$ and the $s_{\mathrm{tissue,high}}/s_{\mathrm{bone}}$ thresholds (denoted by asterisks), respectively.

Figure 4: Orthogonal views of preprocessing steps: (i) Original CT image; (ii) image after intensity-based segmentation into four classes: air (black), low intensity tissue (dark grey), high intensity tissue (light grey) and bone (white); (iii) s_{opened}: the high intensity tissue segmentation image, $s_{\mathrm{tissue,high}}$, after erosion, retention of the largest connected component and dilation; (iv) all three output segmentations: s_{init} (dark grey), $s_{\mathrm{brainstem}}$ (light grey), s_{bone} (white).

Figure 5: (i-iii) Results of applying the illusory surfaces method to three selected images from the dataset. The top row shows a midsagittal slice with the initial segmentations, s_{init}, denoted by black contours and the final ICS segmentation estimations computed by the illusory surfaces method shown as white contours. The curved lines highlight the extent of the frontal fontanelles and show that the segmentation boundaries have been slightly contracted and smoothed. The inferiorly located arrowheads in (i), (ii) (iii) point to locations where the segmentation boundary in the foramen magnum has been smoothed to form a consistent segmentation boundary shape between images. The bottom row shows surface renderings of the final segmentations.

Figure 6: (i) Midsagittal slice of one image in the dataset showing the effect of extreme values of $\beta = 2$ (black) and $\beta = 20$ (inner white contour), with the ground truth segmentation (outer white contour). The over-smoothing effect is particular evident in

highly curved skull sections, such as the orbits which are annotated by a white arrow. (ii) Midsagittal slice of another image of the dataset showing the typical segmentation error where the estimated boundary (white) of the foramen magnum is inferior to the ground truth boundary (black) (see arrowhead). The parameter choices for this figure were ($\beta = 2, \mu = 30$). Note the skulls displayed in this figure are physically distorted by the craniosynostosis, the aspect ratio of these panels is correct.

Figure 7: Midsagittal slice of the image that consistently produced the highest error value across parameter combinations in original orientation (i) and after manual rotation so that the basion/opisthion axis is in the axial plane (ii). The estimated segmentation for ($\beta = 2, \mu = 30$) (white) and ground truth boundary (black) are shown. The largest discrepancy between the ground truth and estimated segmentation boundary in (i) is indicated by the arrow.

TABLE LEGENDS

Table 1: Values of the user-selectable parameters for the illusory surfaces method (μ and β) used in the parameter sweep.

Table 2: The mean (minimum, maximum) Hausdorff distances (HD), in mm, across the 43 images for the first (i) and second (ii) set of manual segmentation images and parameter combination presented in Table 1.

Parameter	Values
μ	10, 20, 30, 40, 50
β	2, 3, 4, 5, 8, 11, 14, 20

Table 1: Values of the user-selectable parameters for the illusory surfaces method (μ and β) used in the parameter sweep.

(i) HD values (in mm) between estimated segmentation boundary and “ground truth” case 1

β \ μ	10	20	30	40	50
2	6.04 (3.24, 13.35)	6.06 (2.76, 13.25)	6.24 (2.80, 13.25)	6.37 (2.97, 13.29)	6.41 (2.87, 13.30)
3	6.07 (3.46, 13.04)	6.08 (2.74, 13.80)	6.12 (3.02, 13.44)	6.23 (2.92, 14.10)	6.34 (2.89, 13.30)
4	6.03 (3.55, 12.46)	6.01 (2.97, 13.35)	6.06 (2.71, 13.01)	6.18 (3.00, 14.60)	6.27 (2.84, 13.90)
5	6.18 (3.72, 13.01)	6.04 (3.31, 14.14)	6.03 (2.74, 13.99)	6.14 (2.87, 13.49)	6.17 (3.04, 13.71)
8	6.51 (4.20, 12.55)	6.11 (3.36, 13.46)	6.20 (3.19, 13.62)	6.28 (3.26, 13.31)	6.32 (3.24, 13.86)
11	6.82 (4.57, 9.31)	6.40 (3.66, 12.49)	6.41 (3.38, 13.69)	6.56 (3.32, 14.63)	6.59 (3.48, 13.76)
14	7.00 (4.59, 12.48)	6.67 (3.95, 12.54)	6.59 (3.46, 12.88)	6.65 (3.39, 13.52)	6.74 (3.46, 14.15)
20	7.63 (4.95, 9.61)	7.01 (4.34, 10.16)	6.92 (3.74, 12.52)	6.92 (3.45, 12.54)	7.01 (3.51, 13.79)

(ii) HD values (in mm) between estimated segmentation boundary and “ground truth” case 2

β \ μ	10	20	30	40	50
2	7.12 (3.39, 12.77)	7.17 (2.87, 13.14)	7.39 (3.03, 13.37)	7.44 (3.39, 13.54)	7.54 (3.61, 13.90)
3	7.11 (3.58, 12.59)	7.03 (3.00, 12.85)	7.14 (2.84, 13.01)	7.34 (2.86, 13.60)	7.40 (3.40, 13.61)
4	7.15 (4.23, 12.67)	7.00 (3.51, 12.82)	7.07 (2.89, 13.21)	7.17 (2.68, 13.02)	7.35 (3.19, 13.70)
5	7.31 (4.17, 12.37)	7.05 (3.58, 12.78)	7.07 (2.90, 13.26)	7.21 (3.13, 13.13)	7.29 (2.81, 13.52)
8	7.89 (4.98, 12.43)	7.25 (3.56, 12.94)	7.23 (3.50, 12.80)	7.41 (3.31, 13.28)	7.40 (3.19, 13.03)
11	8.21 (5.26, 11.91)	7.54 (4.35, 12.08)	7.43 (3.49, 12.76)	7.51 (3.81, 13.12)	7.62 (3.61, 13.03)
14	8.44 (5.59, 12.17)	7.96 (4.45, 12.74)	7.66 (3.94, 12.32)	7.63 (3.79, 13.10)	7.70 (3.67, 13.22)
20	9.16 (5.61, 12.87)	8.31 (5.46, 11.92)	8.12 (4.12, 12.61)	7.96 (3.79, 12.50)	7.94 (4.08, 13.12)

Table 2: The mean (minimum, maximum) Hausdorff distances (HD), in mm, across the 43 images for the first (i) and second (ii) set of manual segmentation images and parameter combination presented in Table 1.

(i)

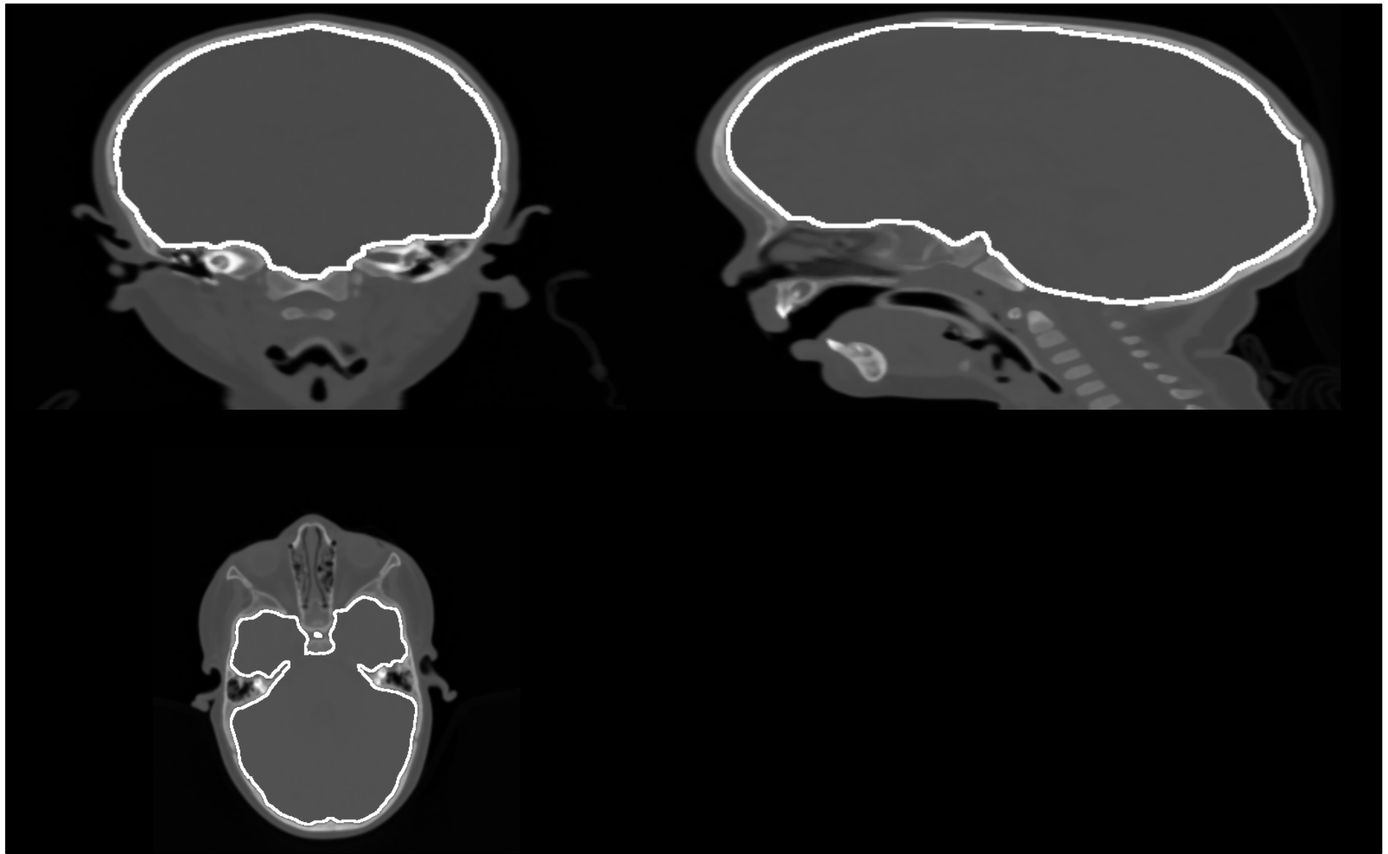

(ii)

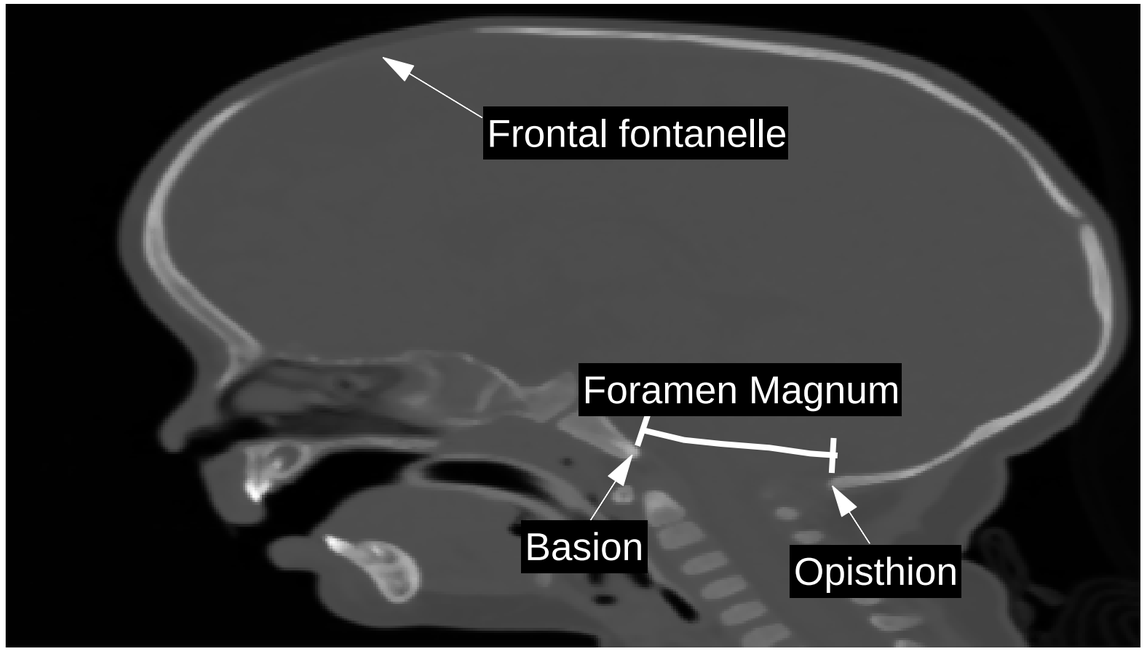

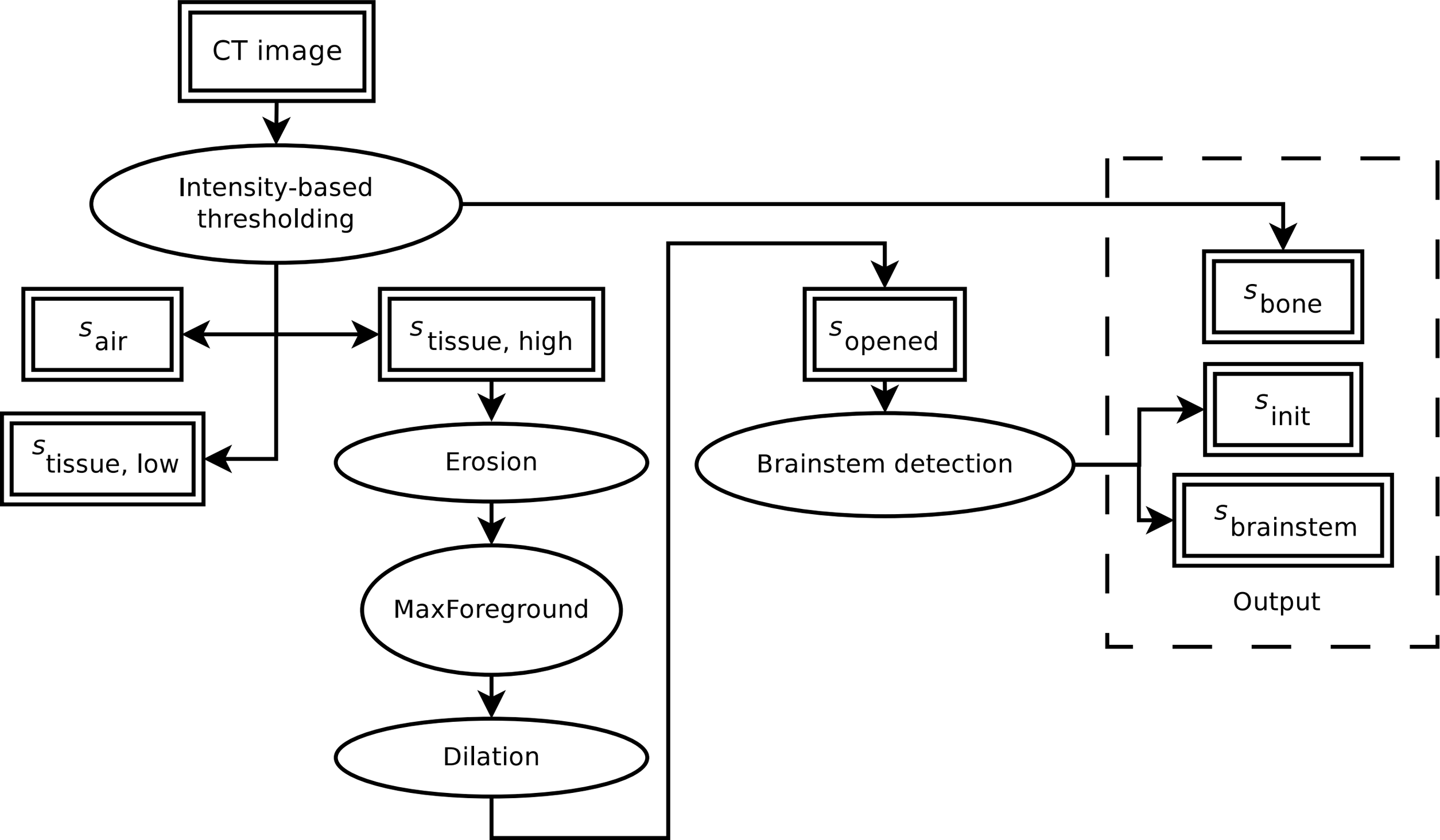
CT image
Intensity-based thresholding
s_{air}
$s_{tissue, high}$
$s_{tissue, low}$
Erosion
MaxForeground
Dilation
s_{opened}
Brainstem detection
s_{bone}
s_{init}
$s_{brainstem}$
Output

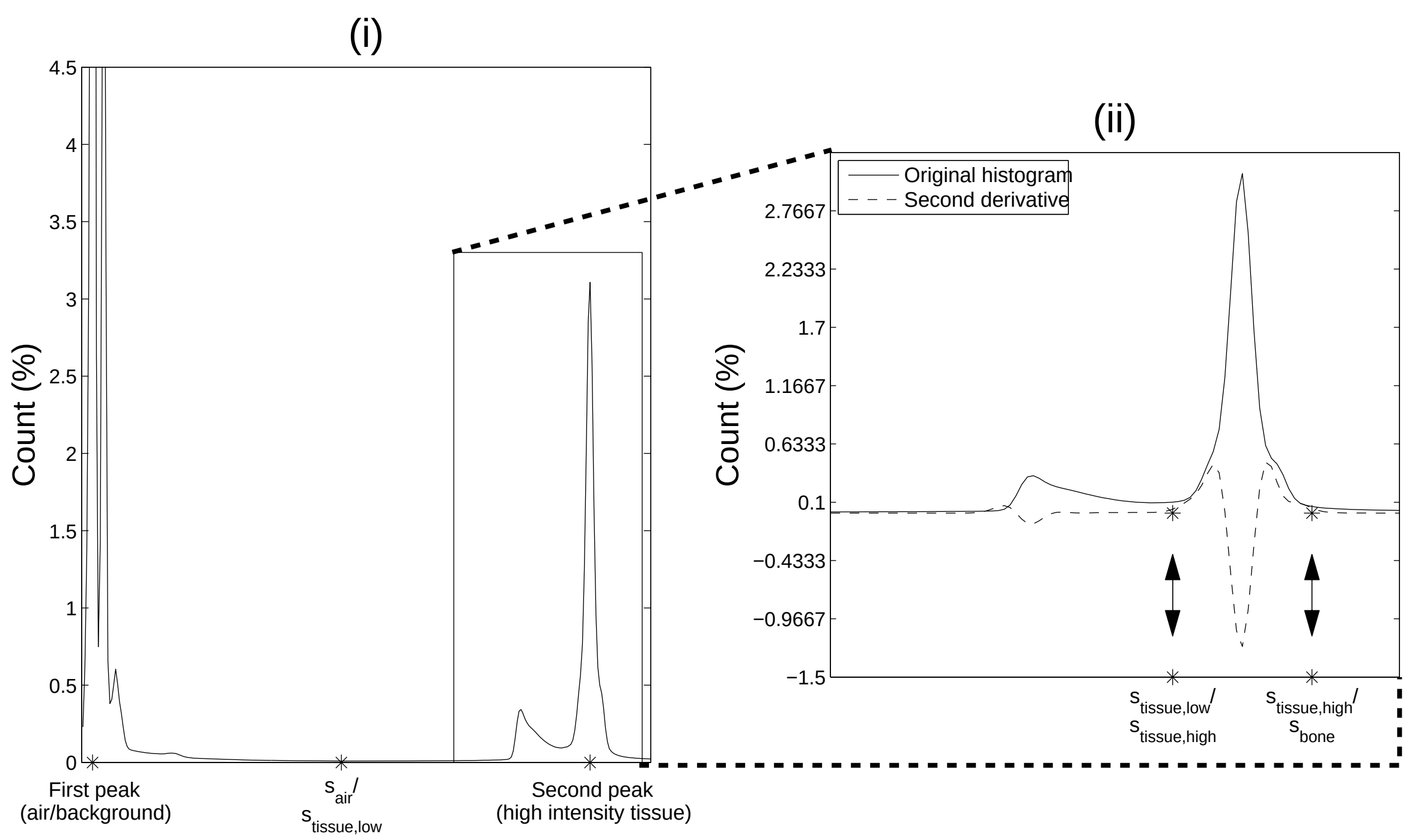
(i)
(ii)
Count (%)
4.5
4
3.5
3
2.5
2
1.5
1
0.5
0
First peak
(air/background)
s_{air} /
$s_{tissue,low}$
Second peak
(high intensity tissue)
Original histogram
Second derivative
2.7667
2.2333
1.7
1.1667
0.6333
0.1
−0.4333
−0.9667
−1.5
$s_{tissue,low}$ /
$s_{tissue,high}$
$s_{tissue,high}$ /
s_{bone}

(i)

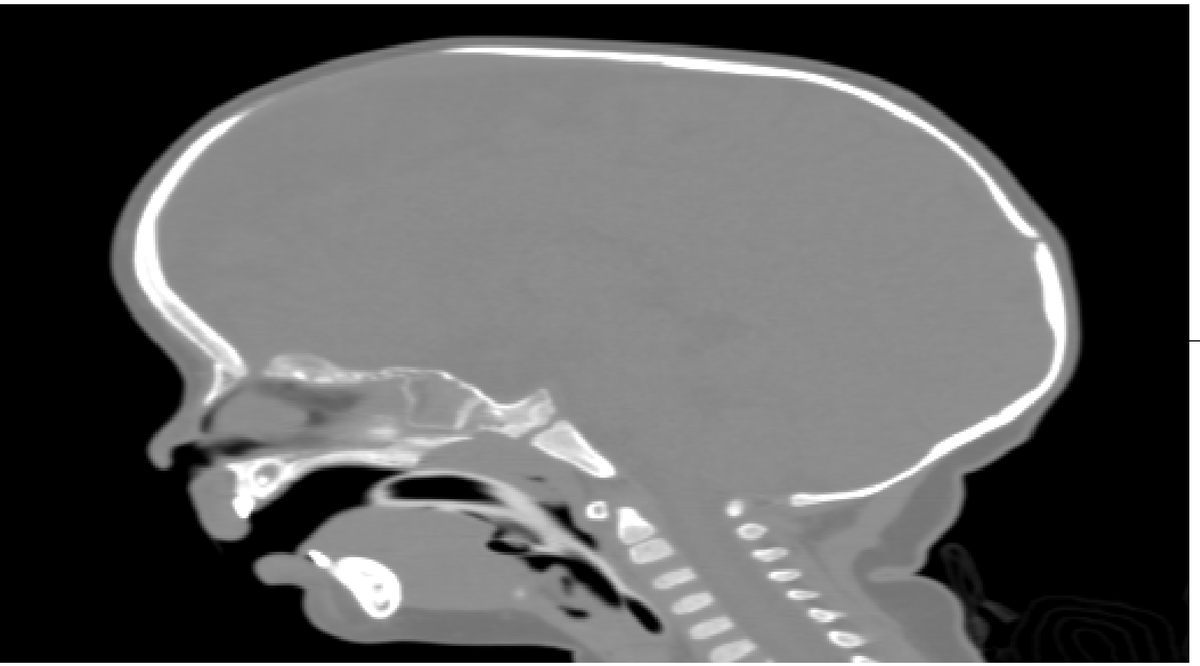

(ii) s_{air}, $s_{tissue,\ low}$, $s_{tissue,\ high}$, s_{bone}

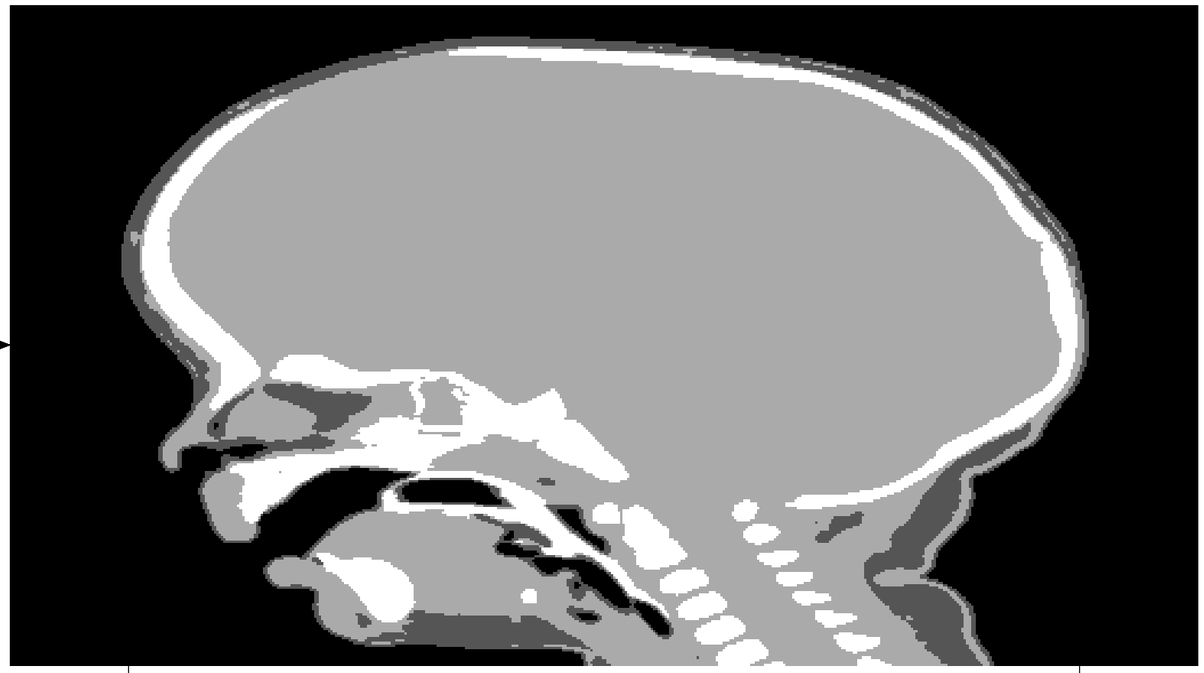

(iii) s_{opened}

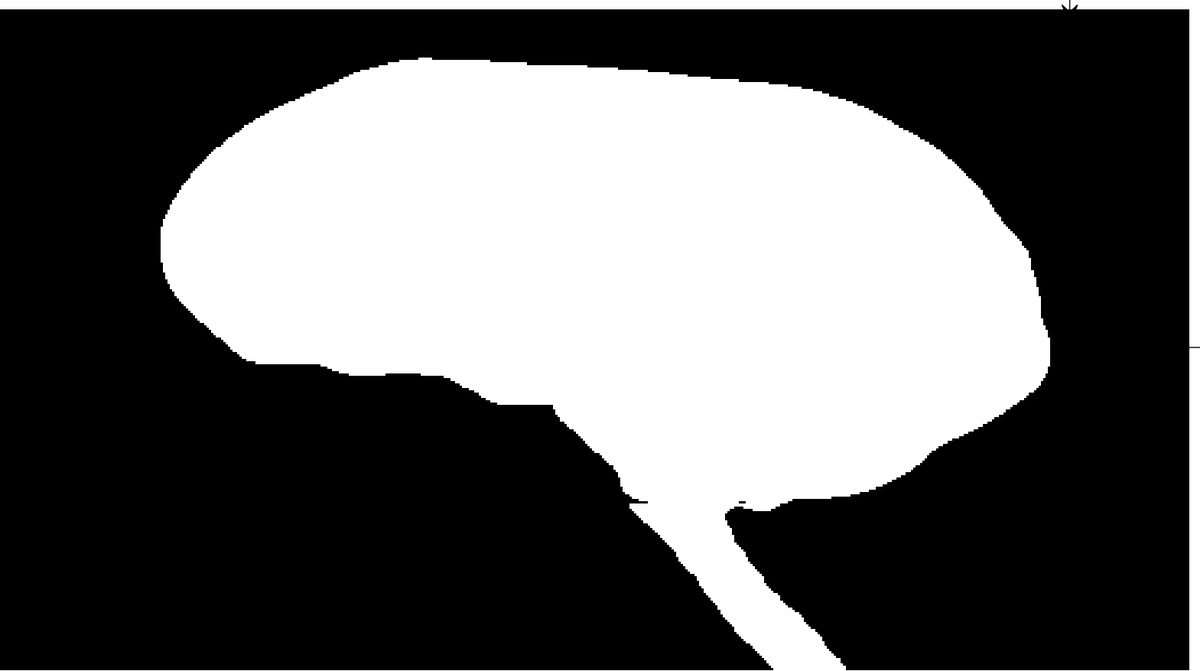

(v) s_{init}, $s_{brainstem}$, s_{bone}

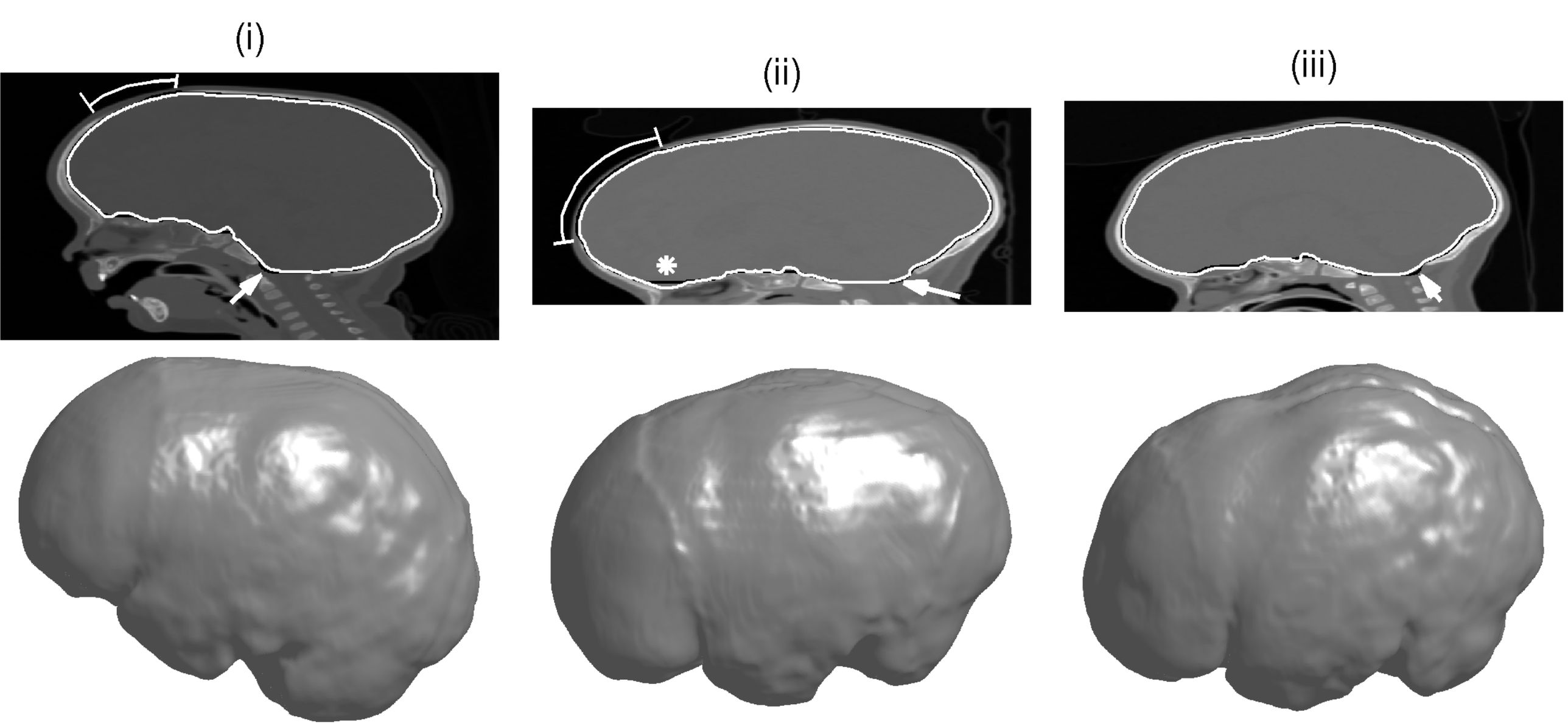
(i)
(ii)
(iii)

(i)

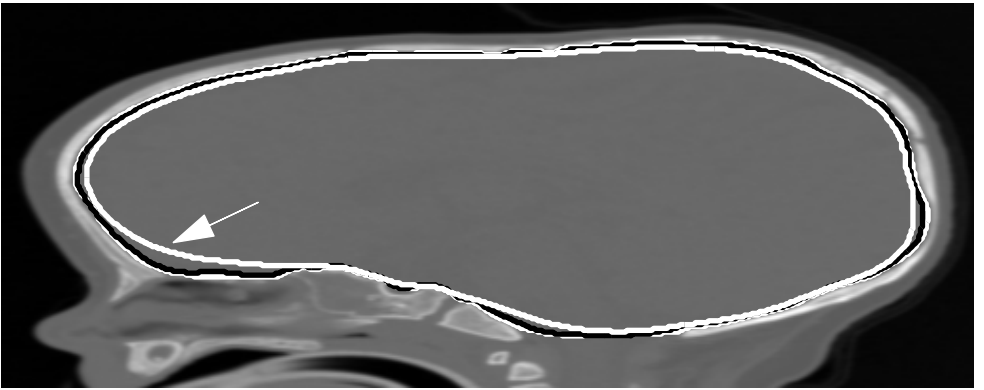

(ii)

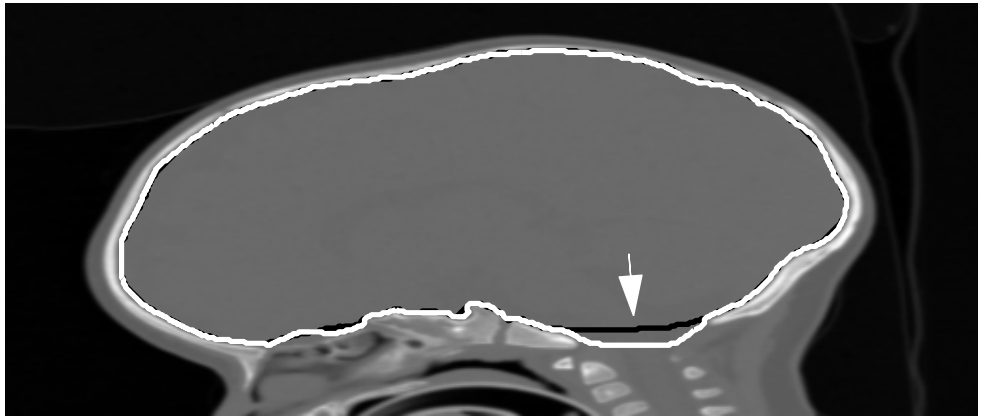

(i)

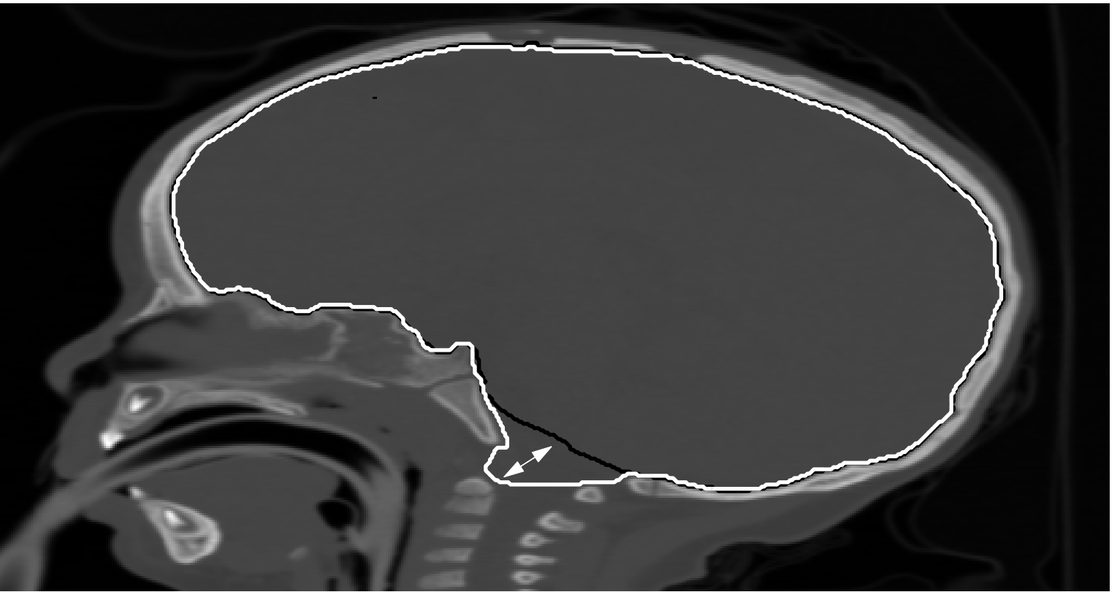

(ii)

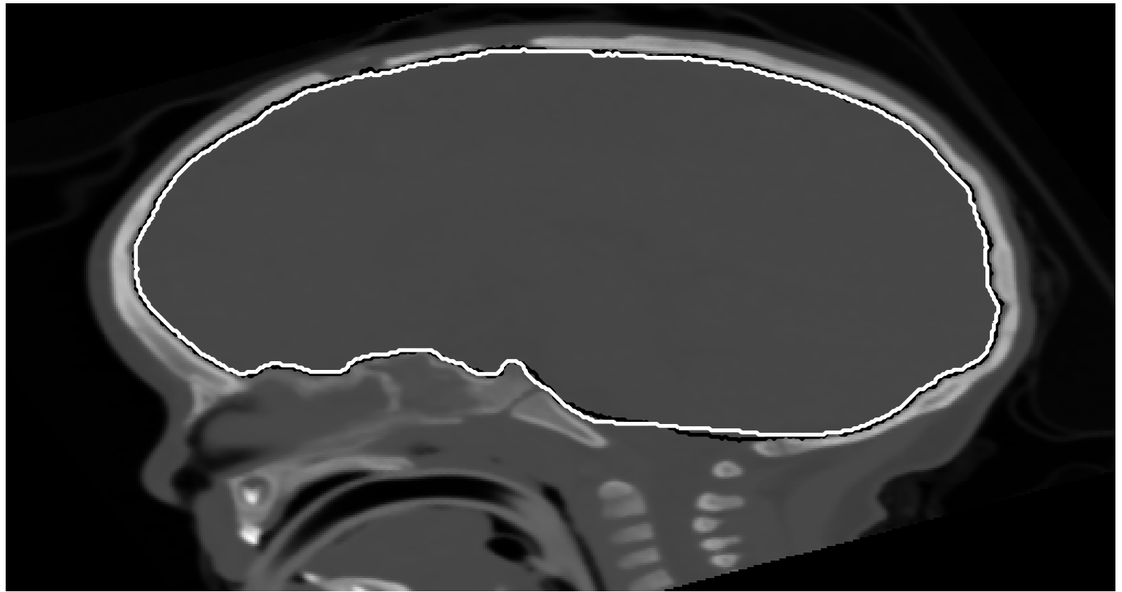

Author/s:
Adamson, C; Da Costa, AC; Beare, R; Wood, AG

Title:
Automatic Intracranial Space Segmentation for Computed Tomography Brain Images

Date:
2013-06-01

Citation:
Adamson, C., Da Costa, A. C., Beare, R. & Wood, A. G. (2013). Automatic Intracranial Space Segmentation for Computed Tomography Brain Images. JOURNAL OF DIGITAL IMAGING, 26 (3), pp.563-571. https://doi.org/10.1007/s10278-012-9529-8.